INORGANIC CHEMISTRY FRONTIERS

RESEARCH ARTICLE

View Article Online
View Journal | View Issue

Cite this: *Inorg. Chem. Front.*, 2025, **12**, 7615

Design rules and experimental validation of carbene–metal–amide luminophores: systematic modification of the amide ligand

Nguyen Le Phuoc,[a] Arun Kumar,[b] Aliaksandr Baidak,[b,c] Alexander S. Romanov*[b] and Mikko Linnolahti*[a]

Received 4th June 2025,
Accepted 29th July 2025

DOI: 10.1039/d5qi01245g

rsc.li/frontiers-inorganic

Carbene–metal–amides (CMAs) have emerged as promising thermally activated delayed fluorescence (TADF) emitters for organic light-emitting diodes (OLEDs). Here, we present a comprehensive computational investigation of amide ligand effects on CMA photophysics, examining *ca.* 70 complexes through density functional theory and its time-dependent extension. Our systematic analysis reveals how structural modifications influence key parameters, including HOMO–LUMO overlap, singlet–triplet energy gaps, oscillator strengths, and metal–ligand bond energies. We demonstrate emission tunability across the visible spectrum through strategic modification of carbazole, indole, carboline, and guanidine-based amides. The computational screening identified promising candidates balancing TADF efficiency with molecular stability. Guided by these predictions, we synthesized two rationally designed complexes with contrasting excited state alignments, and tested their photo- and radioluminescence performance. This combined theoretical–experiment approach establishes clear structure–property relationships for CMA design and demonstrates the effectiveness of computational screening in accelerating OLED material development.

Introduction

Organic light-emitting diodes (OLEDs) have emerged as key components in advanced display technologies and energy-efficient lighting solutions.[1] Among promising OLED emitters, carbene–metal–amides (CMAs)[2–21] offer unique advantages through their tunable emission properties and high efficiency. These complexes feature a two-coordinate coinage metal (Au, Cu, Ag), bridging an electron-accepting carbene and electron donating amide ligand.[2] CMAs achieve high efficiency through thermally activated delayed fluorescence (TADF), which enables harvesting of both singlet and triplet excitons for light emission. In this mechanism, singlet excitons undergo either prompt fluorescence or intersystem crossing (ISC) to form triplet states. These triplet excitons can then absorb thermal energy to undergo reverse ISC (RISC) back to the emissive singlet state, producing delayed fluorescence. The efficiency of this TADF process depends critically on the energy difference between the lowest excited singlet (S_1) and triplet (T_1) states (ΔE_{ST}).[22,23]

Since the introduction of the archetypical CMA1 in 2017,[3] extensive studies have been reported, exploring structural modifications to enhance photophysical properties and OLED performance. On the carbene side, variations in cyclic (alkyl)(amino)carbene (CAAC) structure, including ring size alterations and substituent modifications, have demonstrated significant effects on emission wavelengths and quantum yields. Changes to the carbene π-system through benzannulation have enabled access to deep red emission, while modified ring sizes have influenced emission lifetimes and gaps between the highest occupied molecular (HOMO) and lowest unoccupied molecular (LUMO) orbitals.[4–6] On the amide size, systematic modification of the carbazole core through electron-donating and -withdrawing substituents have achieved emission tuning from yellow to deep blue, with some derivatives showing near-unity quantum yields and sub-microsecond delayed fluorescence lifetimes.[4,7]

Although these experimental studies have demonstrated the versatility of CMA complexes as OLED emitters, a comprehensive understanding of the structure–property relationships governing their photophysical behavior remains elusive. Building on our previous investigation of CAAC effects in CMA emit-

[a]*Department of Chemistry and Sustainable Technology, University of Eastern Finland, Joensuu Campus, FI-80101 Joensuu, Finland. E-mail: mikko.linnolahti@uef.fi*
[b]*Department of Chemistry, The University of Manchester, Oxford Rd, Manchester M13 9PL, UK. E-mail: alexander.romanov@manchester.ac.uk*
[c]*Dalton Cumbrian Facility, The University of Manchester, West Lakes Science Park, Moor Row, CA24 3HA, UK*

ters,[24] we now present a systematic computational study examining how the amide structural modifications influence key photophysical parameters.

Using density functional theory (DFT)[25,26] and time-dependent DFT (TD-DFT),[27] we analyze diverse amide-structural motifs including modified carbazoles, expanded ring systems, and heterocyclic derivatives. Our investigation examines key parameters such as frontier orbital energies, singlet–triplet gaps, oscillator strengths, and bond dissociation energies. The computational analysis guides the synthesis of two rationally designed CMA complexes, demonstrating bright emission in agreement with theoretical predictions. By establishing clear structure–property relationships validated through targeted synthesis, this work provides design principles for high-performance CMA-based OLED materials and demonstrates the effectiveness of computational screening in accelerating emitter development.

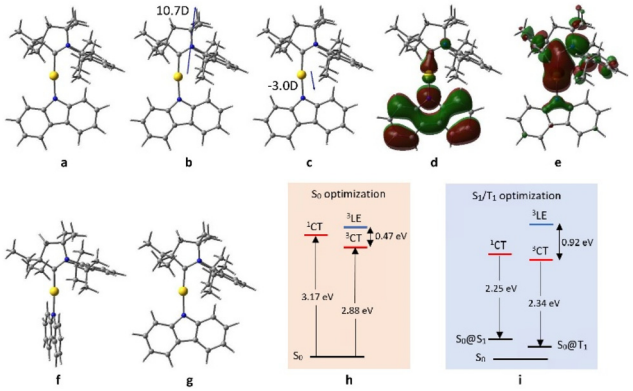

Fig. 1 Computed structures and properties of **e-2-1** complex: (a) optimized ground state S_0 geometry; (b) dipole moments in S_0 and (c) S_1@S_0 state; (d) the HOMO and (e) LUMO orbitals; (f) optimized S_1; (g) optimized T_1; (h) vertical excitation energies indicated by the upward arrows; (i) fluorescence (left) and phosphorescence (right) energies indicated by the downward arrows at optimized S_1 and T_1 geometries.[24]

Computational details

All calculations were performed using Gaussian 16 [28] with the global hybrid MN15 functional[29] and def2-TZVP basis set,[30,31] except the spin–orbit coupling matrix elements (SOCME) were calculated by Orca 6.0.[32] For gold atoms, core electrons were treated using a 60-electron relativistic effective core potential.[33] Ground state geometries were fully optimized without symmetry constraints. Excited states were investigated by TD-DFT,[27] within the Tamm-Dancoff approximation,[34] which helps overcome the typical TD-DFT underestimation of excited states energies.[35,36] The validity of this approach for CMA systems has been previously demonstrated,[8–11] with TD-DFT and unrestricted DFT methods showing only 0.004 eV difference T_1 energies for CMA1.[37] Vertical excitations and oscillator strengths were calculated for all complexes, with excited state geometry optimizations and SOC calculations performed for selected cases of particular interest. Electronic structure analysis included Mulliken population analysis to determine metal contributions to frontier orbitals. HOMO–LUMO overlap integral S evaluates the spatial overlap between frontier molecular orbitals and is calculated as:

$$S = \int \Psi_{\mathrm{HOMO}}(r)\Psi_{\mathrm{LUMO}}(r)\,\mathrm{d}r$$

where Ψ_{HOMO} and Ψ_{LUMO} are the normalized HOMO and LUMO wave functions. This integral was computed using Multiwfn program.[38]

Results and discussion

E-2-1 – The reference complex

Building upon our computational framework, we first analyze the reference complex, **e-2-1**, an ethyl-substituted CAAC (^{Et}CAAC) gold carbazole (Fig. 1), which serves as benchmark for investigating amide modifications. This complex has demonstrated superior performance compared to the original CMA1,[3] exhibiting 99% photoluminescence (PL) quantum yield (PLQY) in toluene, microsecond-scale excited state lifetime, and excellent stability.[24]

The ground state electronic structure reveals characteristic donor–acceptor behavior. The HOMO is predominantly localized on the carbazole amide with minimal (2.8%) gold contribution, while the LUMO distributes across the Au-CAAC moiety with 10.8% metal character (Fig. 1d and e). This orbital arrangement yields a HOMO–LUMO overlap integral of 0.35, favorable for TADF.[39] The complex exhibits a substantial ground state dipole moment (10.7 D) oriented along the C–Au–N axis toward the carbene ligand. Notably, upon vertical excitation to S_1@S_0, the dipole moment not only decreases in magnitude (to 3.0 D) but also reverses direction (Fig. 1b and c). This dramatic reversal change reflects the charge-transfer (CT) nature of the excitation, as electron density shifts from the amide to the carbene moiety and may significantly influence the interaction between the complex and its environment in OLED devices.[40] Vertical excitations analysis shows that both S_0–S_1 and S_0–T_1 transitions are dominated by HOMO-to-LUMO character (>94%), confirming their CT nature. The calculated energies (S_1: 3.17 eV, T_1: 2.88 eV) yield a ΔE_{ST} of 0.29 eV. Notably, the lowest triplet excitation (^{3}LE) localized to the amide ligand (^{3}LE(A)) corresponds to the second lowest excited triplet (T_2) state at 3.35 eV, positioned above the CT states as required for efficient TADF.[41]

Geometry optimization of the excited states reveals significant structural and energetic changes from the ground state. While S_0 and T_1 geometries maintain a near-coplanarity between amide and carbene ligands, the S_1 state prefers a perpendicular arrangement that lies 0.17 eV lower than the coplanar configuration. This structural reorganization has profound implications for the photophysical properties. The ΔE_{ST} gap decreases from 0.29 eV in the vertical excitation to 0.11 eV

when determined from optimized geometries, potentially enhancing RISC efficiency.[42] Simultaneously, the S_1–S_0 oscillator strength undergoes a dramatic reduction, falling from the ground state S_0–S_1 oscillator strength of 0.1952 to zero in the fully relaxed S_1 geometry. The resulting emission energies are 2.25 eV for fluorescence (S_1–S_0@S_1) and 2.34 eV for phosphorescence (T_1–S_0@T_1), reflecting significant Stokes shifts[43] (Fig. 1h and i). The vanishing oscillator strength in the relaxed S_1 geometry, when considered alongside the experimentally observed high PLQY, suggests that emission likely occurs from a higher-energy near-coplanar configuration. The impressive TADF performance of the complex can thus be attributed to its ability to dynamically access geometries that strike a crucial balance between efficient RISC, enabled by the reduced ΔE_{ST} in the perpendicular configuration, and strong radiative transitions from near-coplanar geometries.

Analysis of the structural stability of the complex through bond dissociation energy calculations reveals robust metal–ligand interactions. The Au–C bond exhibits higher strength (403.2 kJ mol^{-1}) compared to the Au–N bond (375.5 kJ mol^{-1}), with the difference (ΔE = 27.7 kJ mol^{-1}) identifying the metal–amide interface as the more vulnerable point for potential degradation. These values indicate overall strong metal–ligand coordination, crucial for maintaining structural integrity under typical OLED operating conditions.[44]

Dataset selection

Building on the promising properties of **e-2-1**, we conducted a systematic investigation of amide modifications in ^{Et}CAAC–Au–amide complexes to establish structure–property relationships. Our design strategy encompassed both validated experimental structures and carefully selected hypothetical derivatives, organized into four main categories (Fig. 2): carbazole substitution patterns, ring-expanded systems, heterocyclic variants, and guanidine-based amides.

1. Carbazole modifications: we systematically functionalized the carbazole's six-membered rings at α, β, γ, and δ positions with diverse substituents including: electron-donating groups (OH, OCH_3), electron-withdrawing groups (CF_3, CN), alkyl groups (CH_3, ^{t}Bu), and halogens (Cl, Br). This comprehensive substitution strategy was motivated by experimental findings showing that ^{t}Bu- and CF_3-substituted carbazoles yield CMA emitters with tunable emission from yellow to deep blue.[7]

2. Ring expansions: we investigated the effect of expanding the carbazole's five-membered ring using heteroatoms (N, O, S) and alkyl groups. Previous work has demonstrated that such modifications enable broad spectral tuning, with PLQYs reaching 89% and successful implementation in yellow, sky-blue, and warm-white OLEDs.[8]

3. Indole and carboline derivatives: following reports of efficient blue emission from azacarbazole-based CMAs,[9] we explored structurally related heterocycles. This series includes indole and carboline cores with established synthetic accessibility (*e.g.* skatole,[45] indoline,[46] harmane,[47] pinoline[48]), allowing for potential experimental validation.

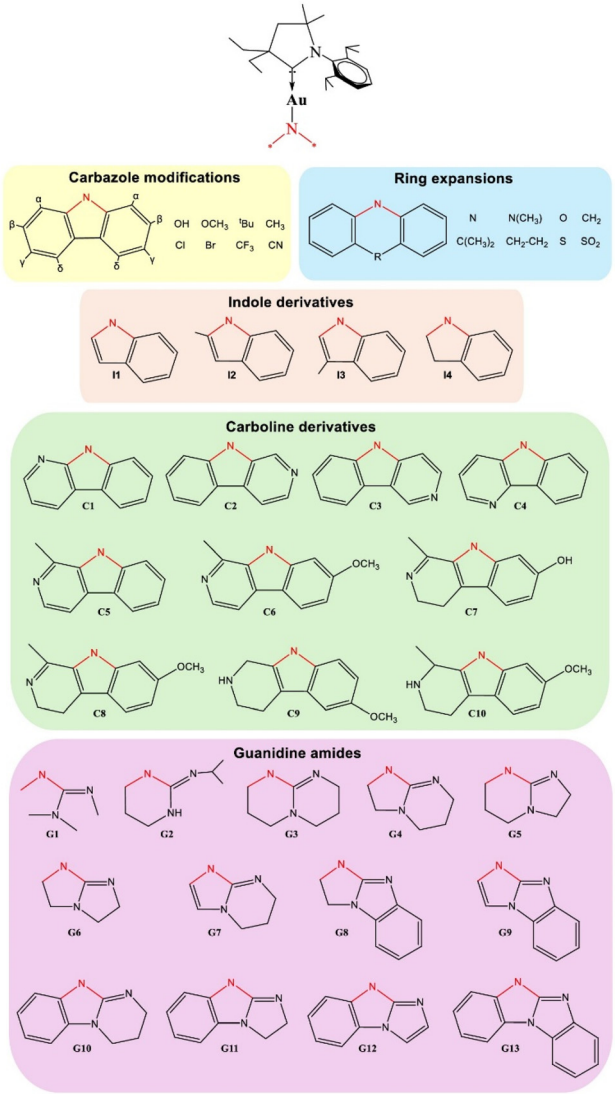

Fig. 2 Structural variations of ^{Et}CAAC–Au–amide complexes investigated in this study, categorized by amide modification type.

4. Guanidine amides: recent demonstrations of exceptional performance of rigid benzoguanidine-based CMAs[10] prompted investigation of related structures. We examined both simple guanidine cores (**G1–G6**) and extended π-systems (**G7–G13**), targeting the promising deep-blue emission (424–466 nm), unity PLQY, and sub-microsecond delayed fluorescence demonstrated experimentally.[10]

Our computational analysis encompassed 70 complexes, providing systematic insights into how amide structural variations influence key PL parameters including excited state energies, HOMO–LUMO characteristics, and charge-transfer properties. This comprehensive investigation establishes design principles for optimizing CMA emitters, as detailed in subsequent sections.

Structural and electronic analysis

We begin our analysis by examining three fundamental electronic parameters: metal orbital contributions, HOMO–LUMO

overlap, metal–ligand bond strengths. These ground state properties provide crucial insights into TADF efficiency, emission characteristics, and device stability.

The gold atom's participation in frontier molecular orbitals varies significantly across the investigated complexes. For the HOMO, primarily localized on the amide ligand, shows Au contributions ranging from 0.0% to 5.4%. The LUMO, distributed over the Au–^{Et}CAAC moiety, typically exhibits larger Au character (10.0%–15.6%). The reference complex **e-2-1** shows moderate Au participation of 2.8% and 10.8% in HOMO to LUMO, respectively.

Systematic modification of the carbazole structure reveals distinct trends in metal orbital contributions. Substitution at the α position generally leads to higher Au participation in frontier orbitals, with complex **α_^{t}Bu** showing the highest LUMO contribution (15.6%) across all studied compounds. The effect of β-substitution depends strongly on electronic character: electron-donating groups at this position (as in **β_OH** and **β_OCH$_3$**) completely eliminate Au contribution to HOMO (0.0%), while electron-withdrawing substituents lead to moderate Au participation (2.8–3.3%). Substitution at γ- and *δ*-positions typically results in lower Au contribution to HOMO (γ: 2.4–3.2%, *δ*: 2.0–2.9%). Ring expansion of the carbazole core maintains moderate HOMO contributions (2.4–4.5%) while showing relatively consistent LUMO participation (11.1%–13.6%). Both indole and carboline derivatives show similar patterns of metal participation, with LUMO contributions (10.2–11.6%) comparable to the reference complex **e-2-1**. Guanidine-based amides exhibit the widest range of HOMO Au contributions (1.1–5.0%) while maintaining typical LUMO participation (10.3–12.2%). Notably, across all modifications, the variation in metal contribution to HOMO *versus* the consistency in LUMO reflects the fundamental electronic structure of CMAs: while the HOMO is predominantly localized on the modified amide ligand, the LUMO distributes across the unchanged Au–^{Et}CAAC moiety.

The HOMO–LUMO overlap integral, crucial for TADF efficiency,[49] varies from 0.15 to 0.45 across our dataset. The reference complex **e-2-1** exhibits a moderate overlap integral of 0.35. Substitution effects are most pronounced at the β position, where electron-donating groups significantly reduce orbital overlap: complexes **β_OH** and **β_OCH$_3$** show the lowest values in our dataset (0.15 and 0.17, respectively). Ring-expanded complexes maintain overlap integrals (0.34–0.39) similar to the reference compound. Among heterocyclic variants, complex **I4** exhibits the highest overlap integral (0.45) in our dataset, while most carboline derivatives show values comparable to **e-2-1**. Guanidine-based amides (**G1–G13**) show moderate to low overlap integrals (0.28–0.37). As amide modifications primarily affect the HOMO while leaving the Au-^{Et}CAAC-centered LUMO largely unchanged, the observed variations in HOMO–LUMO overlap reflect the extent to which different amide structures alter the spatial and energetic characteristics of the HOMO.

To assess potential device stability, we calculated Au–N (amide) and Au–C(carbene) bond dissociation energies. The reference complex **e-2-1** exhibits Au–N and Au–C bond energies of 375.5 and 403.2 kJ mol^{-1}, respectively. Across the series, the Au–N bond shows greater variability (274.7–411.7 kJ mol^{-1}) compared to the Au–C bond (373.7–424.6 kJ mol^{-1}), reflecting its greater sensitivity to amide modifications. Electron-withdrawing substituents generally strengthen both metal–ligand bonds, exemplified by complex **β_CF$_3$** with the highest Au–N bond energy of (411.7 kJ mol^{-1}) among carbazole derivatives. This strengthening can be attributed to the reduction of electron density on the amide nitrogen, enhancing the electrostatic interaction with the gold center. Conversely, electron-donating groups tend to weaken this interaction by increasing electron density on the nitrogen. Ring expansions significantly weaken the Au–N bond (274.7–365.2 kJ mol^{-1}) while maintaining relatively strong Au–C bonds (377.0–416.2 kJ mol^{-1}). This weakening is likely due to electronic effects rather than steric factors, with different heteroatoms or groups in the expanded ring altering the electronic structure of the entire π-system. Indole derivatives (**I1–I4**) show moderate Au–N bond strengths (318.4–378.0 kJ mol^{-1}), while carboline-based complexes (**C1–C10**) maintain stronger metal–ligand bonds (Au–N: 348.0–403.9 kJ mol^{-1}, Au–C: 395.8–412.2 kJ mol^{-1}). Guanidine-based amides (**G1–G13**) exhibit lower Au–N bond energies (299.2–375.1 kJ mol^{-1}) compared to the reference complex, which could be explained by the varying degrees of electron delocalization within the guanidine moiety. The markedly different responses of Au–N *versus* Au–C bonds to amide modifications reflect the localized nature of structural changes: while Au–N interaction is directly influenced by modifications to the amide, the Au–C bond to the unchanged carbene remains relatively stable.

Excitation dynamics

The excited state properties of CMA complexes critically determine their TADF performance and emission characteristics. Our computational analysis reveals that most studied complexes exhibit CT transitions for both S_0–S_1 and S_0–T_1 excitations, dominated by HOMO to LUMO character. This CT character arises from electron migration from the amide-localized HOMO to the Au–carbene centered LUMO. Exceptions appear for cases where electron-withdrawing substituents such as CF_3 are attached on the carbazole ligand, namely the S_0–T_1 transition is characterized by amide-localized (LE(A)), as indicated in Table S1. Higher-lying T_2 states show more diverse behavior: most complexes exhibit LE(A) or mixed CT/LE(A) transitions, while guanidine derivatives with single π-bonds (**G1–G5**) uniquely exhibit mixed CT/LE(C) character involving the carbene ligand. This variation in T_2 character demonstrates how amide modifications can influence higher excited states while maintaining the fundamental CT nature of S_1 and T_1.

Our computational results reveal systematic tuning of excited state energies through structural modification (Fig. 3). S_1 energies span from 2.38 eV in the nitrogen-expanded carbazole complex (**R_N**) to 3.91 eV in the α-substituted complex (**α_CF$_3$**), corresponding to emission wavelengths from 521 nm to 317 nm before accounting for Stokes shift effects. T_1 states

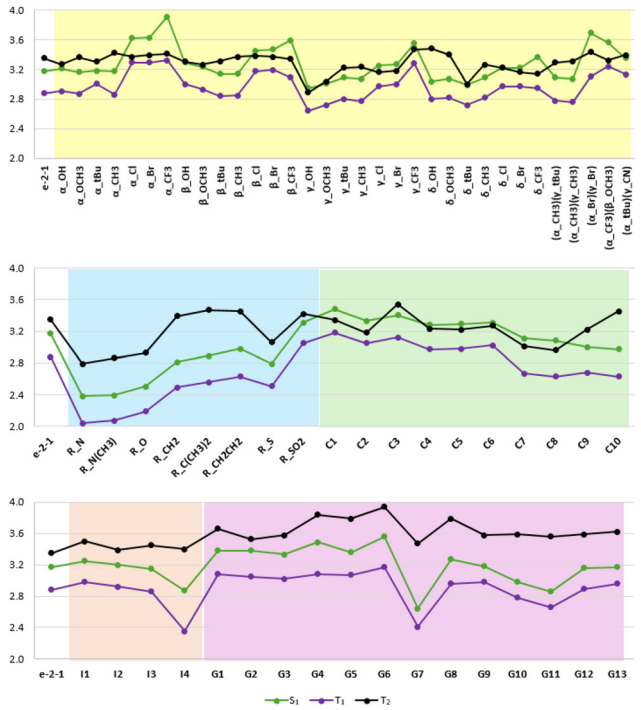

Fig. 3 Vertical excitation energies (eV) of CMA complexes with different amide ligands, including carbazole modifications (yellow), ring expansions (blue), carboline derivatives (green), indole derivatives (orange), and guanidine amides (purple).

follow a similar pattern, ranging from 2.04 eV (**R_N**) to 3.32 eV (**α_CF$_3$**), with S_1/T_1 energy ratios remaining notably consistent between 1.06–1.22 across the series.

Another excited state that warrants careful consideration relative to S_1 and T_1 states is T_2. For efficient TADF, the optimal energetic hierarchy is $T_2 > S_1 > T_1$. This ordering ensures that thermal equilibration occurs primarily between CT states S_1 and T_1, without interference from higher triplet manifolds. If T_2 is positioned energetically below S_1, it may serve as a competing decay channel, thereby disrupting the desired $S_1 \leftrightarrow T_1$ equilibrium essential for TADF. In such cases, excitons in the S_1 state can undergo competing ISC to the lower-lying T_2 state, removing population from the TADF-active S_1 state. Additionally, thermal activation from T_1 to S_1 becomes less favorable when T_2 provides an alternative, lower-energy triplet state. Furthermore, T_2 states often exhibits distinct orbital character, potentially introducing additional non-radiative decay pathway. In the systems under investigation, T_2 state energies (2.79–3.94 eV) typically lie above S_1, thereby supporting favorable conditions for TADF. However, several compounds show T_2 states below their respective S_1 energies. For instance, in **γ_OH**, T_2 (2.89 eV) lies below S_1 (2.95 eV), and similar inversion occurs with many other substitution patterns. This unfavorable energy ordering could compromise TADF efficiency. The occurrence of such cases, particularly with electron-withdrawing substituents, highlights a key molecular design challenge: modifications targeting blue emission through raised S_1 energies must simultaneously maintain appropriate excited state ordering.

Analysis of other structural modifications reveals distinct trends in excited state ordering. Ring-expanded complexes maintain favorable $T_2 > S_1$ ordering, with **R_N** and **R_N(CH$_3$)** exhibiting the lowest S_1 energies in our dataset (2.38–2.39 eV), though the series extends to higher energies up to 3.31 eV in **R_SO$_2$**. Indole derivatives (**I1–I4**) similarly preserve T_2 above S_1 with substantial gaps (T_2–$S_1 \geq 0.19$ eV), though at typically higher S_1 energies (2.87–3.25 eV). Carboline derivatives, despite their promise as blue emitters with S_1 energies up to 3.48 eV, show several cases of unfavorable energy ordering, particularly in **C7** and **C8**, where T_2 lies below S_1 by 0.10–0.12 eV. In contrast, guanidine-based complexes (**G1–G13**) consistently maintain T_2 above S_1 across a wide range of S_1 energies (2.64–3.56 eV), suggesting this modification strategy may be particularly robust for maintaining appropriate state ordering while tuning emission wavelength.

The TADF-critical ΔE_{ST} gap and S_0–S_1 oscillator strength show systematic variation with structural modification (Fig. 4). Among carbazole derivatives, α-substitution produces the widest range of ΔE_{ST} values, from **α_^{t}Bu** (0.17 eV) to **α_CF$_3$** (0.59 eV). Ring expansions generally maintain moderate ΔE_{ST} gaps (0.26–0.35 eV), while guanidine derivatives, particularly **G9–11** and **G13**, achieve consistently small gaps (0.20–0.21 eV). These variations correlate with HOMO–LUMO overlap inte-

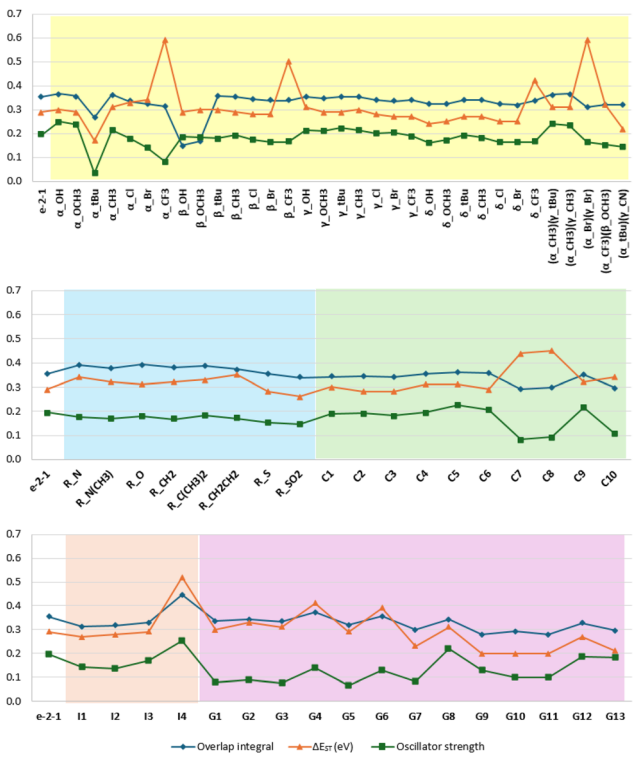

Fig. 4 Comparison between overlap integral, ΔE_{ST}, and oscillator strength of CMA complexes with different amide ligands, including carbazole modifications (yellow), ring expansions (blue), carboline derivatives (green), indole derivatives (orange), and guanidine amides (purple).

grals: complexes with smaller overlaps typically show reduced ΔE_{ST} gaps but often at the cost of diminished oscillator strength. Notably, **β_OH** and **β_OCH$_3$** show minimal overlaps (0.15–0.17) and moderate ΔE_{ST} (0.29–0.30 eV), with reasonably high oscillator strengths (≈0.19), but their nearly degenerate S_1 and T_2 states ($\Delta E \approx 0.03$ eV) may complicate TADF performance. Complex **γ_^{t}Bu** maintains moderate overlap integral (0.35) and achieves high oscillator strength (≈0.22) while keeping ΔE_{ST} manageable (0.29 eV), with favorable T_2–S_1 gap of 0.13 eV. However, despite promising ΔE_{ST} (0.31 eV) and high oscillator strength (≈0.23), carboline derivative **C5** shows unfavorable state ordering with T_2 (3.22 eV) below S_1 (3.29 eV). These results highlight the multiple requirements for efficient TADF emitter design: optimal complexes must balance moderate ΔE_{ST} gaps for efficient RISC, maintain sufficient oscillator strength for strong radiative decay, and crucially, preserve favorable excite state ordering with T_2 above S_1.

Electrostatic dipole moments provide insight into potential reorganization energies and TADF efficiency.[40] Ground state dipole moments in all complexes align along the C(carbene)–Au–N(amide) axis towards the carbene, mirroring **e-2-1** (10.7 D), but with magnitudes varying widely (4.1–17.0 D). Notably, guanidine-based complexes (**G1–G6**) show the smallest S_0 dipole moments (4.1–5.4 D), while some γ- and δ-substituted carbazoles exhibit the largest (*e.g.* **δ_CF$_3$** with 17.0 D; **γ_Cl**, **γ_Br**, and **γ_CF$_3$** with 14.2–16.0 D). Upon S_0–S_1 excitation, most complexes exhibit a reversal in dipole moment direction, consistent with CT character, and often a significant change in magnitude. The S_1@S_0 dipole moments range from −8.0 D to 4.9 D. Large changes are observed in complexes like (**α_CF$_3$**) (**β_OCH$_3$**) (from 8.0 D to −7.2 D) and **γ_Br** (from 14.5 D to −0.8 D). These substantial reorganizations of charge distribution may impact TADF performance through enhanced non-radiative decay or altered solid-state packing interactions.[40]

Structure–property relationships

Our comprehensive study reveals intricate relationships between structural modifications and key photophysical properties of CMA complexes. We analyze these relationships across various structural motifs. Table 1 and **S2** illustrate comparative analysis providing valuable insights into distinct trends in how different amide structures affect calculated parameters.

Carbazole α-substitution offers the widest tunability but with important trade-offs for TADF design. Electron-donating groups (OH, OCH_3, ^{t}Bu) maintain favorable HOMO–LUMO overlap and reduce ΔE_{ST} gaps, supporting efficient RISC, while enhancing oscillator strength for bright emission. However, electron-withdrawing groups (CF_3, Cl, Br) achieve substantial blue-shifts (up to 3.91 eV) but at the cost of increased ΔE_{ST} gaps (up to 0.59 eV) and reduced oscillator strength. The α-position shows the strongest electronic coupling to the metal center, with **α_^{t}Bu** exhibiting the highest Au contribution to frontier orbitals (15.6% LUMO). For blue emission applications, α-substitution requires careful balance between achieving target energies and maintaining TADF efficiency.

β-substitution provides unique electronic control through dramatic HOMO–LUMO decoupling. Electron-donating groups (**β_OH**, **β_OCH$_3$**) create the most spatially separated donor–acceptor systems in our dataset (overlap integrals 0.15–0.17), potentially enabling very small ΔE_{ST} gaps while maintaining reasonable oscillator strengths (*ca.* 0.19). However, their nearly degenerate S_1 and T_2 states may complicate TADF dynamics. Electron-withdrawing groups offer substantial blue-shifts (up to 3.59 eV with **β_CF$_3$**) while preserving electronic coupling, making this position ideal for high-energy blue emitters. Uniquely among all positions, β-substitution universally strengthens metal–ligand bonds, suggesting enhanced operational stability for device applications.

Table 1 Comparative analysis of the general effect of the amide structure on calculated parameters related to PL characteristic

	Carbazole modifications				Ring expansions	Indole derivatives (I1–I4)	Carboline derivatives (C1–C10)	Guanidine amides (G1–G13)
	α-substitution	β-substitution	γ-substitution	δ-substitution				
%Au/HOMO	↗ ↗	~/↘ ↗	~/↘ ↗	↘ ↘	↗	↘	~/↗/↘	↗ ↘
%Au/LUMO	↗ ↗	~ ↗	~ ~	~ ~	↗	~	~/↗	↗ ~
Overlap integral	↗ ↘	~/↘ ~	~ ~	↘ ↘	~/↗	↘	~/↘	~ ↘
S_1 energy	~/↗ ↗	~/↗ ↗	↘ ↗	↘ ↗	↘	↗	↗/↘	↗ ↘
ΔE_{ST}	~/↘ ↗	~ ↗	~ ↘	↘ ↗	↗	~	~/↗	↗ ↘
Oscillator strength	↗ ↘	↘ ↘	↗ ↗	↘ ↘	↘	↘	~/↗/↘	↘ ↘
S_0 dipole moment	↘ ↘	↘ ↘	↘ ↗	↘ ↗	↘	↘	↗/↘	↘ ↘
S_1@S_0 dipole moment	↗ ↗	↗ ↗	↗ ↘	↗ ↘	↘	↗	↗	↗ ↗
Au–N bond dissociation energy	↘ ↗	↗ ↗	↘ ↗	↘ ↗	↘	~/↘	↗/↘	↘ ↘
Au–C bond dissociation energy	↘ ~	↗ ↗	↘ ↗	~ ↗	↘	↘	~/↗	↘ ~/↗

↗ increasing, ↘ decreasing, ~ maintaining,/or. Red color: electron-donating group. Blue color: electron-withdrawing group. Green color: guanidine amide with one π bond (**G1–G6**). Purple color: guanidine amide with increasing conjugation (**G7–G13**).

γ-substitution emerges as the "sweet spot" for TADF optimization, offering emission tuning without compromising key electronic parameters. Unlike other positions, γ-substitution maintains consistent HOMO–LUMO overlap (0.34–0.36) and favorable ΔE_{ST} gaps (0.27–0.31 eV) across all substituents, while uniquely preserving or enhancing oscillator strength. Complex **γ_^{t}Bu** exemplifies this balance with high oscillator strength (0.22), moderate ΔE_{ST} (0.29 eV), and favorable T_2–S_1 ordering. The position enables systematic emission tuning (2.95–3.55 eV) while maintaining TADF-critical parameters, making it ideal for fine-tuning emission color without sacrificing efficiency.

δ-substitution offers similar benefits to γ-substitution but with enhanced ΔE_{ST} control. Electron-donating groups achieve the smallest ΔE_{ST} gaps in the carbazole series (**δ_OH**: 0.24 eV), making this position attractive for maximizing RISC efficiency. However, electron-withdrawing groups produce detrimental large gaps (**δ_CF$_3$**: 0.42 eV) with reduced oscillator strength, limiting blue emission applications. The position provides a viable alternative to γ-substitution when minimal ΔE_{ST} is prioritized over oscillator strength, though the latter trade-off must be carefully considered for overall TADF performance.

Ring expansion of the five-membered carbazole ring provides the most dramatic red-shifts in our dataset but with significant stability trade-offs. Nitrogen incorporation (**R_N**, **R_N(CH$_3$)**) achieves the lowest S_1 energies (2.38–2.39 eV) for accessing orange-red emission, while maintaining favorable ΔE_{ST} gaps for TADF. However, these systems suffer from substantially weakened Au–N bonds (274.7–277.1 kJ mol^{-1} *vs.* 375.5 kJ mol^{-1} reference) and reduced oscillator strength, potentially compromising device stability and brightness. The **R_SO$_2$** system offers a compromise, approaching reference S_1 energy while providing the smallest ΔE_{ST} gap (0.26 eV) in the series. Ring expansion is most suitable for red-shifted emission applications where the stability trade-offs are acceptable.

Indole derivatives split into two distinct categories with contrasting design implications. Complexes **I1–I3** maintain TADF-favorable properties similar to the reference (ΔE_{ST}: 0.27–0.29 eV, S_1: 3.15–3.25 eV) but with reduced oscillator strength, making them suitable for blue emission with moderate brightness. In stark contrast, **I4** represents an outlier with the highest HOMO–LUMO overlap in our dataset (0.45) and enhanced oscillator strength (0.25), but suffers from a prohibitively large ΔE_{ST} gap (0.52 eV) that likely prevents efficient TADF. The indole scaffold offers a reliable platform for blue emitters (**I1–I3**), while **I4** serves as a cautionary example of how structural modifications can disrupt TADF balance.

Carboline derivatives demonstrate how nitrogen position critically affects TADF performance, creating two distinct design pathways. The **C5–C6** series achieves excellent oscillator strength (0.20–0.23) with moderate ΔE_{ST} gaps, making them promising blue emitters despite slightly unfavorable T_2 ordering. Conversely, **C7–C8** suffer from poor oscillator strength (0.08–0.09) and large ΔE_{ST} gaps (0.44–0.45 eV), effectively eliminating TADF capability. The carboline scaffold offers high-performance blue emission potential (**C5**, **C6**) but requires careful nitrogen positioning to avoid TADF-detrimental configurations. Enhanced metal–ligand bonding across the series suggests improved stability compared to other heterocyclic modifications.

Guanidine amides reveal how π-conjugation extent fundamentally determines emitter performance, creating two complementary design strategies. Single π-bond systems (**G1–G6**) target deep-blue emission (3.33–3.56 eV) but suffer from large ΔE_{ST} gaps (up to 0.41 eV) and poor oscillator strength, limiting TADF efficiency. Extended conjugation systems (**G7–G13**) unlock exceptional TADF performance with small ΔE_{ST} gaps (0.20–0.21 eV) and tunable emission (2.64–3.27 eV), with **G13** demonstrating optimal balance (ΔE_{ST}: 0.21 eV, oscillator strength: 0.18). The guanidine platform offers a unique design lever – π-extension – to transition from stable blue phosphors (**G1–G6**) to high-performance TADF emitters (**G7–G13**).

Implications and design strategy

The systematic structure–property analysis reveals a clear hierarchy of design strategies for optimizing CMA emitters. For emission tuning, γ-substitution emerges as the most versatile approach, offering systematic color control (2.95–3.55 eV) without compromising TADF parameters, while ring expansion provides access to deep-red emission when stability trade-offs are acceptable. For maximizing TADF efficiency, β-electron-donating groups and guanidine π-extension (**G7–G13**) achieve the smallest ΔE_{ST} gaps, while α-electron-donating groups optimize oscillator strength. For blue emission applications, carboline **C5–C6** types and γ-/δ-electron-withdrawing substitutions provide high-energy access with maintained efficiency, avoiding problematic configurations like **C7–C8** or **I4**.

Based on this framework, computational screening identifies five leading candidates that exemplify optimal design principles. Complex **γ_^{t}Bu** demonstrates the γ-position advantage with balanced parameters across all metrics: moderate ΔE_{ST} (0.29 eV), high oscillator strength (0.22), and favorable T_2–S_1 ordering. **α_OH** achieves the highest oscillator strength in our dataset (0.25) while maintaining blue emission capability (3.21 eV). Carboline **C6** balances strong emission properties (oscillator strength: 0.20) with enhanced stability, though T_2 positioning requires consideration. Guanidine complexes **G12** and **G13** represent the success of the π-extension strategy, combining small ΔE_{ST} gaps (0.21–0.27 eV) with robust $T_2 > S_1$ ordering essential for uncompromised TADF.

To validate these computational predictions and understand the emission mechanisms, excited state geometry optimizations were performed for all five candidates. The optimized structures (Fig. 5) reveal distinct photophysical behaviors that explain their relative performance. Complexes **γ_^{t}Bu**, **C6**, **G12**, and **G13** exhibit the expected TADF-favorable rotation from coplanar S_0/T_1 geometries to perpendicular S_1 configuration, reducing ΔE_{ST} to 0.11–0.20 eV (Table 2). This rotation mechanism enables thermal $S_1 \leftrightarrow T_1$ equilibration essential for TADF, though requiring geometric reorganization (0.06–0.17 eV) to achieve maximum oscillator strength for emission. In contrast, **α_OH** demonstrates why α-substitution

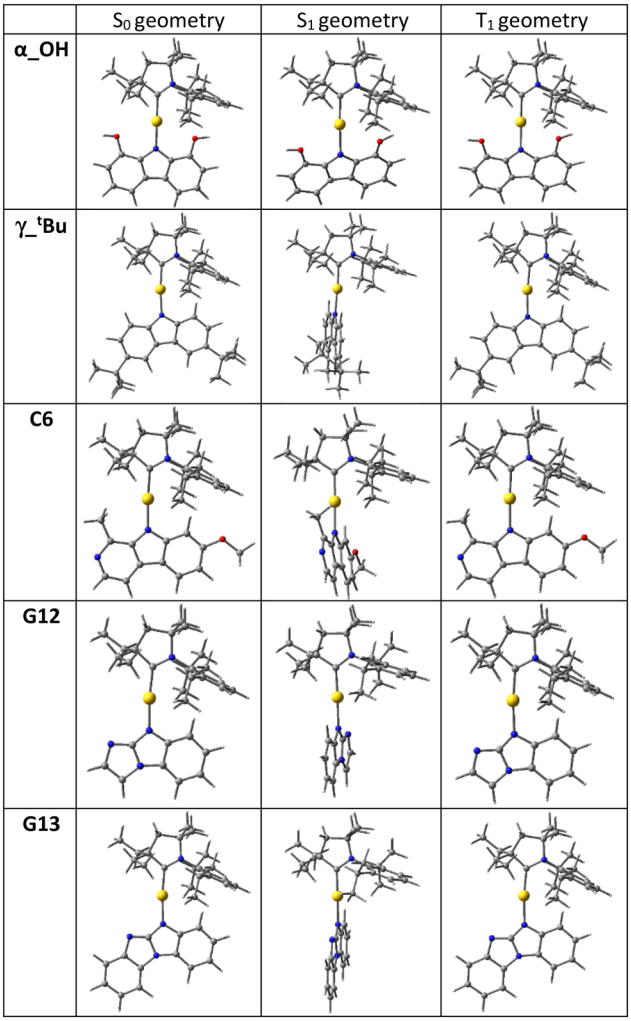

Fig. 5 S_0, S_1, and T_1 optimized geometries.

requires careful design consideration: steric constraints from the proximal hydroxyl group prevent S_1 rotation, maintaining coplanar geometry and resulting in a large ΔE_{ST} (0.26 eV) that impedes RISC. All complexes maintain beneficial ^{3}LE positioning (3.13–3.37 eV) above CT states, confirming appropriate excited state ordering for TADF applications.

Spin–orbit coupling analysis provides additional mechanistic insight into these performance differences. The calculated SOCMEs between ^{1}CT and ^{3}CT states reveal significant variations across the series (3.65–100.79 cm^{-1}, Tables 2 and S3). Complex **α_OH** exhibits the highest SOCME (100.79 cm^{-1}), indicating rapid ISC from singlet to triplet state. However, its large ΔE_{ST} (0.26 eV) and inability to adopt the perpendicular S_1 geometry hinder efficient RISC, negatively impacting TADF performance. In contrast, **γ_^{t}Bu**, **C6**, **G12**, and **G13** show significantly smaller SOCMEs (3.65–6.20 cm^{-1}) combined with favorable small ΔE_{ST} gaps (0.11–0.20 eV) that enable efficient RISC. Notably, **G13** achieves optimal balance with the smallest SOCME (3.65 cm^{-1}) and ΔE_{ST} gaps (0.12 eV), consistent with its superior experimental TADF performance (*vide infra*). These results suggest that moderate SOC strength is preferable for CMA emitters, providing sufficient ISC/RISC rates while minimizing competing non-radiative decay pathways.

Synthesis and testing of promising candidates

Following our computational analysis identifying **C6** and **G13** as promising candidates, the closely related complexes **C5** and **G13** (Fig. 6) were synthesized and fully characterized to validate our theoretical predictions. Complex **C5** represents an excellent structural analogue of **C6** with nearly identical calculated properties, providing effective experimental validation of our computational framework. Both complexes are obtained from the (^{Et2}CAAC)AuCl and benzoguanidine (**G13**) or harmane (**C5**) in the presence of the KO^{t}Bu base in high yields. All complexes are off-white solids having high stability in air for months and good solubility in polar organic solvent while only sparingly soluble in hexane. Both **C5** and **G13** have been characterised by ^{1}H and ^{13}C NMR (Fig. S1–S4) and high-resolution mass spectroscopy. The thermal stability of the complexes was evaluated with thermogravimetric analysis (TGA, under nitrogen). The decomposition temperature (T_d) for gold complex **C5** is 273 °C and 303 °C for **G13** which is close similar to 304 °C for analogous carbazolide complex **e-2-1**.

Table 2 S_1 and T_1 excited state optimizations and SOCME

		α_OH	γ_^{t}Bu	C6	G12	G13
Vertical S_1 excitation energy (eV)		3.21	3.09	3.31	3.16	3.17
Vertical T_1 excitation energy (eV)		2.91	2.80	3.02	2.89	2.96
ΔE_{ST} [a] (eV)		0.30	0.29	0.29	0.27	0.21
Energy relative to optimized S_0 (eV)	Optimized coplanar S_1	2.84	2.81	3.02	2.79	2.84
	Optimized rotated S_1	2.87	2.64	2.95	2.66	2.78
	Optimized coplanar T_1	2.58	2.53	2.75	2.52	2.66
ΔE_{ST} [b] (eV)		0.26	0.11	0.20	0.14	0.12
^{3}LE energy[c] (eV)		3.15	3.13	3.14	3.28	3.37
Maximum S_1–S_0 oscillator strength[d]		0.0820	0.1670	0.1518	0.1136	0.1322
Fluorescence (S_1–S_0@S_1) (eV)		2.13	2.16	2.32	2.05	2.31
Phosphorescence (T_1–S_0@T_1) (eV)		2.18	2.24	2.45	2.08	2.31
^{1}CT and ^{3}CT SOCME (cm^{-1})		100.79	3.77	4.03	6.20	3.65

[a] Vertical S_1 and T_1 excitations. [b] Optimized S_1 and T_1 geometries. [c] Optimized T_1 geometry. [d] Carbene and amide fixed coplanar.

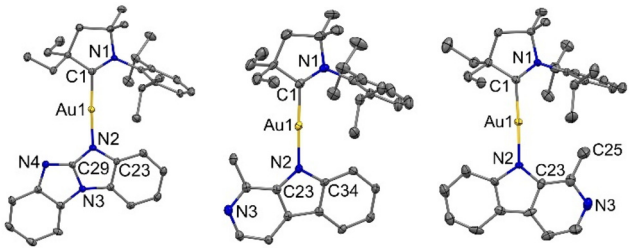

G13
Au–C1 1.981(5) Å
Au–N2 2.020(4) Å
Torsion angle 3.0(1)°
N1–C1–N2–C23

C5 Molecule A
Au–C1 1.978(6) Å
Au–N2 2.031(4) Å
Torsion angle 3.2(1)°
N1–C1–N2–C23

C5 Molecule B
Au–C1 1.984(5) Å
Au–N2 2.034(4) Å
Torsion angle 10.7(1)°
N1–C1–N2–C23

Fig. 6 Single crystal X-ray structure for complex **G13** (left) and two independent molecules A (middle) and B (right) for complex **C5**. The ellipsoids are shown at 50% probability while H atoms are omitted for clarity.

The molecular structure for CMA complexes **C5** and **G13** were confirmed by single crystal X-ray diffraction (Fig. 6). Both **C5** and **G13** have a similar linear geometry for the gold atom with negligible deviation up to 2° from the ideal 180° angle for linear geometry. Unlike complex **e-2-1** [24] having a C_{2v} symmetry for carbazolide amide donor moiety, complexes **C5** and **G13** possess unsymmetrically substituted amide donor. This results in crystallization of the complex **C5** with two independent molecules A and B in the unit cell which are different by conformation of the ethyl-group for the ^{Et}CAAC–carbene π-acceptor ligand and relative orientation with the amide π-donor ligand. For instance, molecule B possesses methyl C-atom C25 pointed towards the center of the 2,6-diisopropylaniline moiety of carbene whereas C25 positioned in the space between of two ethyl groups of the carbene for molecule A. Complex **G13** has only one independent molecules in the unit cell. Both Au–C and Au–N bond lengths for **C5** and **G13** are up to 0.02 Å longer compared to benchmark complex **e-2-1**, indicating greater separation between donor and acceptor ligands for the new CMA materials and influencing their photophysical behaviour, *vide infra*. The torsion angle (C1–N1–N2–C23, Fig. 6) between carbene and carbazole ligands varies in the range from 3.0(1) to 10.7(1)° which is close for complex **e-2-1** (*ca.* 15.1(1)°), indicating near co-planar orientation of the ligands. Analysis of the intermolecular interactions between neighbouring molecules of complexes **C5** and **G13** reveals only weak C–H···π and C–H···N contacts resulting in formation of the 3D-network.

The redox behaviour of complexes **C5** and **G13** was analysed in THF solution with profiles shown in Fig. S6 and data collected in Table S5. Both complexes exhibit a quasi-reversible, carbene ligand-centred reduction process at $E_{1/2}$ value at −2.80 V. All oxidation processes are centered on the amide and irreversible with E_p values at *ca.* +0.46 V (Table S5). This results in close similar values for LUMO at *ca.* 2.70 eV for both complexes but slightly more stabilised HOMO energy level at −5.66 eV for **C5** compared to −5.56 eV for **G13**. The UV-vis absorption spectra in solvents with different polarity (Fig. S5, Table S4) show two major absorption bands: high-energy (*ca.* 300 nm) and low-energy absorption (*ca.* 360 nm) band. Complex **C5** exhibits only well-resolved and narrow absorption bands for both high- and low-energy absorption bands with no solvatochromism effect. We ascribed both bands to π–π* transition localised on the amide-donor ligand, indicating absence of the low energy CT band. Unlike **C5**, complex **G13** possesses a broad L(M)L CT low-energy absorption band, which experience 25 nm blue-shift from methylcyclohexane (MCH) to dichloromethane (DCM, Fig. S5, Table S4). Such a negative solvatochromism for complex **G13** is characteristic for the CMA materials having bright TADF emission mechanism, *vide infra*.

The PL spectra were measured in neat crystals and polystyrene (PS) matrix at 295 K and 77 K (Table 3 and Fig. 7). Both complexes **C5** and **G13** emit blue light at 451 and 460 nm, respectively, which is up to 31 nm blue-shift compared with the **e-2-1** in PS matrix[24] (484 nm, Table 3). The PL profile for harmane complex **C5** possesses poorly resolved vibronic structure (Fig. 7a top) which is becoming apparent upon cooling to 77 K (Fig. 7a bottom). Unlike **C5**, PS films of benzoguanidinato complex **G13** possess a broad CT profile at all temperatures from 295 K to 16 K (Fig. 7b) thus demonstrating the PL behaviour similar to complex **e-2-1**. The CT-state energy for complexes **C5** and **G13** was estimated at *ca.* 3.06 eV from the blue onset of the PL profile in PS matrix at 295 K (Table 3). The excited state lifetime of benzoguanidinato CMA complex **G13** is 0.38 μs which is three orders of magnitude shorter compared to harmane complex **C5** (up to 298 μs) and nearly two-time shorter compared to carbazolide CMA complex **e-2-1** (*ca.* 1.0 μs). Complex **G13** possesses a radiative rate of 2.6×10^6 s^{-1}

Table 3 Photophysical properties of **e-2-1**,[24] **C5** and **G13** complexes in various media

	λ_{em} (nm)	τ (μs)	Φ^a (%)	$k_r{}^b$(10^5 s^{-1})	$k_{nr}{}^c$(10^5 s^{-1})	CT/^{3}LE(A)/$\Delta E_{ST}{}^d$ (eV)	λ_{em} (nm, 77 K)	τ (μs, 77 K)
MeTHF frozen glass								
C5	—	—	—	—	—	—/2.87	450	2522
G13	—	—	—	—	—	—/3.33	402	67 (90%), 1100 (10%)
Polystyrene Matrix (1 wt%)								
e-2-1	484	1.07	82	7.66	1.68	2.92/2.95/−0.03	458	48.0 (63%), 188.3 (32%)
C5	451	40 (30%), 298 (70%)	40	0.02	0.03	3.06/2.87/+0.19	449	401 (44%), 1162 (32%)
G13	460	0.38	99	26	0.26	3.07/3.33/-0.26	448	55

[a] Quantum yields determined using an integrating sphere. [b] Radiative rate constant $k_r = \Phi/\tau$. [c] Nonradiative constant $k_{nr} = (1 - \Phi)/\tau$. [d] CT/^{3}LE(A) energies based on the onset values of the emission spectra blue edge in MeTHF glasses at 77 K and 295 K.

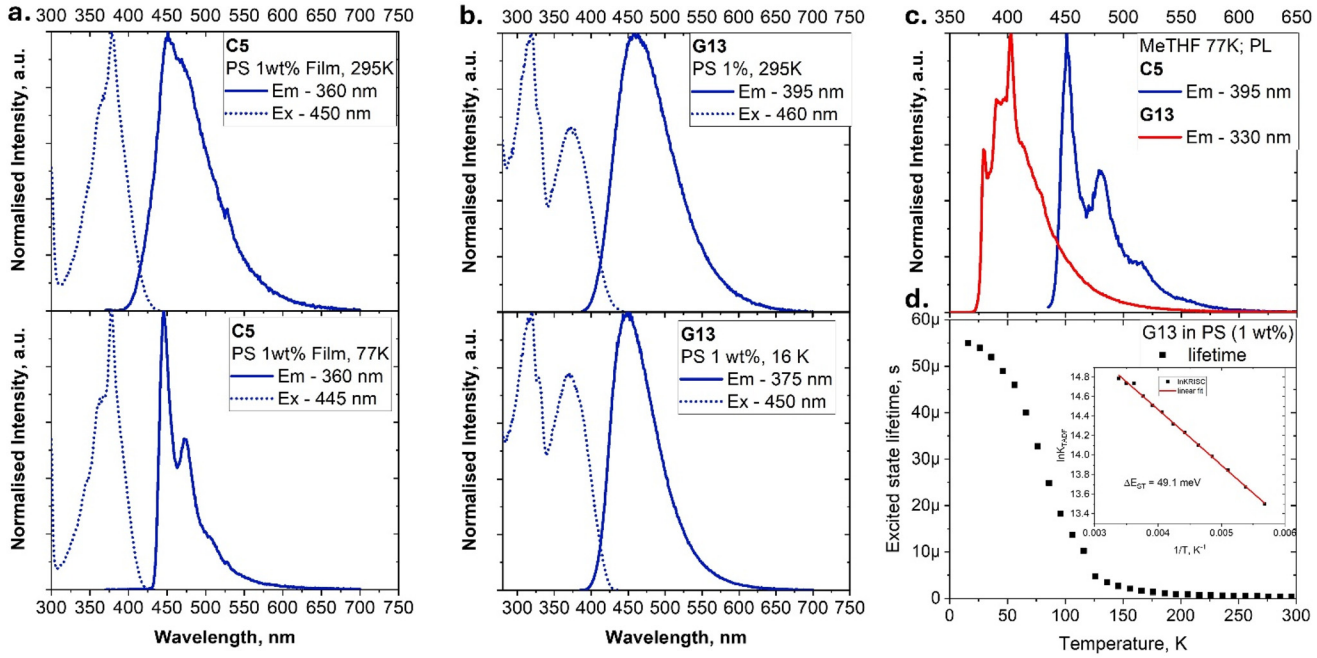

Fig. 7 PL (em – emission; ex – excitation spectrum) of **C5** (a) and **G13** (b) in PS matrix with 1% concentration by weight at 295 K (top), and 77 K or 16 K (bottom). The emission profiles in MeTHF frozen glass at 77 K, revealing a contribution of the ^{3}LE(A) phosphorescence (c); excited state lifetime *vs.* temperature plot for **G13** in PS matrix (d) and Arrhenius plots of $\ln(k_{TADF})$ *vs.* $1/T$ and fitted according to equation: $\ln(k_{TADF}) = \ln(b) - \left(\frac{\Delta E_{ST}}{k_B}\right)\frac{1}{T}$.

which is two-orders of magnitude faster compared to **C5** (2×10^4 s^{-1}, Table 3) thanks to a short excited state lifetime and near unity PLQY for **G13** and only 40% PLQY for **C5**. Such drastic differences in PL performance clearly indicate a different luminescence mechanism governing the PL behaviour of the complexes **C5** and **G13**.

To reveal the energy of the ^{3}LE state, we performed the PL spectra for both complexes in 10^5M MeTHF frozen glass at 77 K (Fig. 7c). Both complexes possess a vibronically resolved PL profile indicative of a dominant phosphorescence from the ^{3}LE(A) at 2.87 eV for **C5** and 3.33 eV for **G13**. Both complexes possess the excited state lifetime in millisecond range supporting assignment of the phosphorescence at 77 K and in line with our previous observations for CMA complexes emitting phosphorescence from the locally excited triplet ^{3}LE(A).[10] The energy difference between CT and ^{3}LE(A) states, ΔE_{ST}, is larger for compound **G13** (−0.26 eV) compared with **C5** (+0.19 eV), while ^{3}LE(A) state is higher in energy compared with CT state for **G13** (Table 3). Such experimental observation unequivocally corroborates our theoretical calculations above. For instance, complex **G13** has the same excited CT and LE-states orientation with the reference compound **e-2-1** (see Fig. 1), where triplet ^{3}LE state is a T_2 state laying above the CT singlet S_1 and triplet T_1. Theoretical calculations predict the energy of the triplet ^{3}LE(A) to be 3.37 eV and energy gap of −0.21 eV (Table 2) which is in excellent agreement with the experimental value of 3.33 eV for ^{3}LE(A) and −0.26 eV for the energy gap in complex **G13**. Therefore, theory and experiment enabled us to assign TADF emission mechanism for the complex **G13**. We also performed a variable-temperature lifetime measurement to estimate the activation energy barrier, ΔE_a, for **G13** in PS film. On cooling to 16 K, the PL profile remains broad and unstructured (Fig. 7b and d) while the emissive lifetime increases from 0.38 μs at 295 K to 55 μs at 16 K (Table 3, Fig. 7d). The ΔE_a for **G13** was estimated as 49.1 meV by an Arrhenius plot analysis of the varied temperature data with $\ln k_{TADF}$ *vs.* $1/T$, supporting high radiative rate of TADF.

Theoretical calculations for complex **C5** predicted that both CT and ^{3}LE(A) triplets are below in energy compared to CT singlet S_1 state. This may result in a mixed character emission from CT and ^{3}LE states simultaneously which is in a good agreement with the experimental observation for PS film of **C5** – a rather broad CT emission profile with features of vibronic structure even at room temperature (Fig. 7a, Table 3).

Spectacular photophysical characteristics for complex **G13** (unity PLQY and short excited state lifetime of 380 ns) spurred our interest to test the applied potential of **G13** in radioluminescence experiment. This is important for development of the advanced scintillators for detecting high-energy X-ray radiation (radioluminescence, RL). Crystals of **G13** were irradiated in an X-ray cabinet at 350 kV (max) and 11.4 mA current, with emission spectra measured using a fibre-optic cable connected to a fluorimeter. Complex **G13** exhibits a RL emission spectra similar to its PL profile (Fig. 8). Radiostability was assessed by monitoring emission intensity at the compound's emission maxima every 10 seconds during constant irradiation at 16.357 Gy min^{-1} (total dose *ca.* 980 Gy). Complex **G13** shows excellent stability with LT_{75} = 1 h (where LT_{75} represents the time required for RL intensity to decrease by 25% under constant

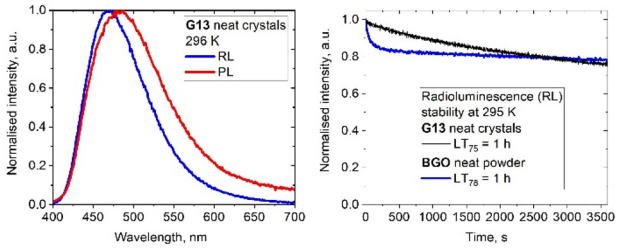

Fig. 8 Overlay of photoluminescence (PL, excited at 360 nm) and radioluminescence emission spectra for **G13** (left); emission intensity decay for **G13** and BGO (industry standard sample) under constant 350 kV X-ray irradiation (right).

350 kV X-ray radiation). The radioluminescence stability for complex **G13** sample is comparable with the industrial standard BGO (bismuth germanium oxide, powder sample) as shown in Fig. 8.

Conclusions

This work presents a comprehensive computational investigation of amide ligand effects on CMA photoluminescence properties, examining approximately 70 complexes to establish structure–property relationships critical for OLED applications. Our systematic analysis reveals how specific structural modifications – from carbazole substitutions to heterocyclic variations – influence key photophysical parameters that determine emission properties and device performance. The study demonstrates that efficient TADF requires precise control of multiple interdependent factors: HOMO–LUMO overlap, S_1–T_1 energy gap, oscillator strength, and metal–ligand bond strengths. Importantly, T_2 state positioning relative to S_1 is crucial for preventing competing decay pathways, while high bond dissociation energies support operational stability.

Our computational screening reveals remarkable emission tunability across the visible spectrum (2.38–3.91 eV), with systematic trends in how structural modifications affect emission energy. Electron-withdrawing substituents on carbazole consistently blue-shift emission, while electron-donating groups show position-dependent effects: ring expansions and extended π-conjugation provide routes to red-shifted emission, while minimal π-systems enable access to blue regions.

The predictive power of our computational approach is validated through the successful synthesis of two rationally designed complexes, **C5** and **G13**, which exhibit bright phosphorescence and TADF emission, respectively, as predicted by their calculated electronic structures. These complexes, strategically selected for their contrasting excited-state alignments, demonstrate how computational insight can guide the targeted development of high-performance emitters. Complex **G13** shows superior deep-blue TADF luminescence with radiative rates up to 2.6×10^6 s^{-1} enabling excellent radioluminescence stability under constant 350 kV X-ray radiation.

This combined theoretical–experimental study establishes a robust framework for CMA emitter design, providing clear guidelines for optimizing TADF performance through structural modification. The validated computational methodology offers an efficient pathway for screening candidate structures before synthesis, accelerating the development of next-generation OLED materials. These insights advance the broader goal of achieving highly efficient, stable, and color-tunable displays and lighting devices based on TADF technology.

Author contributions

Conceptualization, A. S. R. and M. L.; methodology, A. S. R. and M. L.; investigation, N. L. P.; resources, A. S. R. and M. L.; writing—original draft preparation, N. L. P.; synthesis A. K.; crystallography and PL characterization A. K. and A. S. R.; radioluminescence A. B.; writing—review and editing, A. S. R. and M. L.; visualization, N. L. P.; supervision, A. S. R. and M. L. All authors have read and agreed to the published version of the manuscript.

Conflicts of interest

There are no conflicts to declare.

Data availability

The data supporting this article have been included as part of the SI.

Calculated parameters and experimental details, coordinates of optimized structures, cif-files and check CIF for complexes **C5** and **G13**. See DOI: **https://doi.org/10.1039/d5qi01245g**.

CCDC 2454948 and 2454949 contain the supplementary crystallographic data for this paper.[50a,b]

Acknowledgements

DFT computations were made possible by use of the Finnish Grid and Cloud Infrastructure resources (urn:nbn:fi:research-infras-2016072533). N. L. P. acknowledges the Doctoral Programme in Science, Forestry and Technology (Lumeto, University of Eastern Finland), decision 401/2023. A. S. R acknowledges the support from the Royal Society (grant no. URF\R1\180288, RGF\EA\181008, URF\R\231014), EPSRC (grant code EP/K039547/1 and APP46952). M. L. acknowledges the Academy of Finland Flagship Programme, Photonics Research and Innovation (PREIN), decision 320166. We thank Dr Louise Natrajan, EPSRC and University of Manchester for access the Centre for Radiochemistry Research National Nuclear User's Facility (NNUF, EP/T011289/1) to use FLS-1000 fluorometer.

References

1 B. Geffroy, P. Roy and C. Prat, Organic light-emitting diode (OLED) technology: materials, devices and display technologies, *Polym. Int.*, 2006, **55**, 572–582.
2 J. Eng, S. Thompson, H. Goodwin, D. Credgington and T. J. Penfold, Competition between the heavy atom effect and vibronic coupling in donor–bridge–acceptor organometallics, *Phys. Chem. Chem. Phys.*, 2020, **22**, 4659–4667.
3 D. Di, A. S. Romanov, L. Yang, J. M. Richter, J. P. Rivett, S. Jones, T. H. Thomas, M. A. Jalebi, R. H. Friend, M. Linnolahti, M. Bochmann and D. Credgington, High-performance light-emitting diodes based on carbene-metal-amides, *Science*, 2017, **356**, 159–163.
4 R. Hamze, J. L. Peltier, D. Sylvinson, M. Jung, J. Cardenas, R. Haiges, M. Soleilhavoup, R. Jazzar, P. I. Djurovich, G. Bertrand and M. E. Thompson, Eliminating nonradiative decay in Cu(I) emitters: >99% quantum efficiency and microsecond lifetime, *Science*, 2019, **363**, 601–606.
5 R. Jazzar, M. Soleilhavoup and G. Bertrand, Cyclic (Alkyl)- and (Aryl)-(amino)carbene Coinage Metal Complexes and Their Applications, *Chem. Rev.*, 2020, **120**, 4141–4168.
6 F. Chotard, V. Sivchik, M. Linnolahti, M. Bochmann and A. S. Romanov, Mono- versus Bicyclic Carbene Metal Amide Photoemitters: Which Design Leads to the Best Performance?, *Chem. Mater.*, 2020, **32**, 6114–6122.
7 P. J. Conaghan, C. S. B. Matthews, F. Chotard, S. T. E. Jones, N. C. Greenham, M. Bochmann, D. Credgington and A. S. Romanov, Highly efficient blue organic light-emitting diodes based on carbene-metal-amides, *Nat. Commun.*, 2020, **11**, 1758.
8 A. S. Romanov, S. T. E. Jones, Q. Gu, P. J. Conaghan, B. H. Drummond, J. Feng, F. Chotard, L. Buizza, M. Foley, M. Linnolahti, D. Credgington and M. Bochmann, Carbene metal amide photoemitters: tailoring conformationally flexible amides for full color range emissions including white-emitting OLED, *Chem. Sci.*, 2020, **11**, 435–446.
9 A.-P. M. Reponen, F. Chotard, A. Lempelto, V. Shekhovtsev, D. Credgington, M. Bochmann, M. Linnolahti, N. C. Greenham and A. S. Romanov, Donor N-Substitution as Design Principle for Fast and Blue Luminescence in Carbene-Metal-Amides, *Adv. Opt. Mater.*, 2022, **10**, 2200312.
10 A. C. Brannan, H.-H. Cho, A.-P. M. Reponen, S. Gorgon, N. L. Phuoc, M. Linnolahti, N. C. Greenham and A. S. Romanov, Deep-Blue and Fast Delayed Fluorescence from Carbene–Metal–Amides for Highly Efficient and Stable Organic Light-Emitting Diodes, *Adv. Mater.*, 2024, **36**, 2404357.
11 A. S. Romanov, S. T. E. Jones, L. Yang, P. J. Conaghan, D. Di, M. Linnolahti, D. Credgington and M. Bochmann, Mononuclear Silver Complexes for Efficient Solution and Vacuum-Processed OLEDs, *Adv. Opt. Mater.*, 2018, **6**, 1801347.
12 P. J. Conaghan, S. M. Menke, A. S. Romanov, S. T. E. Jones, A. J. Pearson, E. W. Evans, M. Bochmann, N. C. Greenham and D. Credgington, Efficient Vacuum-Processed Light-Emitting Diodes Based on Carbene–Metal–Amides, *Adv. Mater.*, 2018, **30**, 1802285.
13 A. S. Romanov, L. Yang, S. T. E. Jones, D. Di, O. J. Morley, B. H. Drummond, A.-P. M. Reponen, M. Linnolahti, D. Credgington and M. Bochmann, Dendritic Carbene Metal Carbazole Complexes as Photoemitters for Fully Solution-Processed OLEDs, *Chem. Mater.*, 2019, **31**, 3613–3623.
14 S. Shi, M. C. Jung, C. Coburn, A. Tadle, M. R. D. Sylvinson, P. I. Djurovich, S. R. Forrest and M. E. Thompson, Highly Efficient Photo- and Electroluminescence from Two-Coordinate Cu(I) Complexes Featuring Nonconventional N-Heterocyclic Carbenes, *J. Am. Chem. Soc.*, 2019, **141**, 3576–3588.
15 R. Hamze, S. Shi, S. C. Kapper, D. S. M. Ravinson, L. Estergreen, M.-C. Jung, A. C. Tadle, R. Haiges, P. I. Djurovich, J. L. Peltier, R. Jazzar, G. Bertrand, S. E. Bradforth and M. E. Thompson, "Quick-Silver" from a Systematic Study of Highly Luminescent, Two-Coordinate, d^{10} Coinage Metal Complexes, *J. Am. Chem. Soc.*, 2019, **141**, 8616–8626.
16 M. B. Gildner and T. W. Hudnall, Cyclic (aryl)(amido)carbenes: pushing the π-acidity of amidocarbenes through benzannulation, *Chem. Commun.*, 2019, **55**, 12300–12303.
17 M. Gernert, L. Balles-Wolf, F. Kerner, U. Müller, A. Schmiedel, M. Holzapfel, C. M. Marian, J. Pflaum, C. Lambert and A. Steffen, Cyclic (Amino)(aryl)carbenes Enter the Field of Chromophore Ligands: Expanded π System Leads to Unusually Deep Red Emitting CuI Compounds, *J. Am. Chem. Soc.*, 2020, **142**, 8897–8909.
18 J. Feng, E. J. Taffet, A.-P. M. Reponen, A. S. Romanov, Y. Olivier, V. Lemaur, L. Yang, M. Linnolahti, M. Bochmann, D. Beljonne and D. Credgington, Carbene-Metal-Amide Polycrystalline Materials Feature Blueshifted Energy yet Unchanged Kinetics of Emission, *Chem. Mater.*, 2020, **32**, 4743–4753.
19 J. Hossain, R. Akhtar and S. Khan, Luminescent coinage metal complexes of carbenes, *Polyhedron*, 2021, **201**, 115151.
20 Q. Gu, F. Chotard, J. Eng, A.-P. M. Reponen, I. J. Vitorica-Yrezabal, A. W. Woodward, T. J. Penfold, D. Credgington, M. Bochmann and A. S. Romanov, Excited state lifetime modulation by twisted and tilted molecular design in carbene-metal-amide photoemitters, *Chem. Mater.*, 2022, **34**(16), 7526–7542.
21 A. Ying and S. Gong, A Rising Star: Luminescent Carbene-Metal-Amide Complexes, *Chem. – Eur. J.*, 2023, **29**, e202301885.
22 H. Uoyama, K. Goushi, K. Shizu, H. Nomura and C. Adachi, Highly efficient organic light-emitting diodes from delayed fluorescence, *Nature*, 2012, **492**, 234–238.
23 Y. Liu, C. Li, Z. Ren, S. Yan and M. Bryce, All-organic thermally activated delayed fluorescence materials for organic light-emitting diodes, *Nat. Rev. Mater.*, 2018, **3**, 18020.
24 N. L. Phuoc, A. C. Brannan, A. S. Romanov and M. Linnolahti, Tailoring Carbene–Metal–Amides for

Thermally Activated Delayed Fluorescence: A Computationally Guided Study on the Effect of Cyclic (Alkyl)(amino)carbenes, *Molecules*, 2023, **28**, 4398.
25 J. Callaway and N. H. March, Density Functional Methods: Theory and Applications, *Solid State Phys.*, 1984, **38**, 135–221.
26 R. G. Parr and W. Yang, *Density-Functional Theory of Atoms and Molecules*, Oxford University Press, Oxford, 1989.
27 F. Furche and D. Rappoport, Density Functional Methods for Excited States: Equilibrium Structure and Electronic Spectra. in *Computational Photochemistry*, ed. M. Olivuccim, Elsevier, Amsterdam, Netherlands, 2005, 16, 93–128.
28 M. J. Frisch, G. W. Trucks, H. B. Schlegel, G. E. Scuseria, M. A. Robb and J. R. Cheeseman and *et al.*, *Gaussian 16*, Revision A. 03, Gaussian Inc., Wallingford CT, USA, 2016.
29 H. S. Yu, X. He, S. L. Li and D. G. Truhlar, MN15: A Kohn–Sham global-hybrid exchange–correlation density functional with broad accuracy for multi-reference and single-reference systems and noncovalent interactions, *Chem. Sci.*, 2016, **7**, 5032–5051.
30 F. Weigend, M. Häser, H. Patzelt and R. Ahlrichs, RI-MP2: optimized auxiliary basis sets and demonstration of efficiency, *Chem. Phys. Lett.*, 1998, **294**, 143–152.
31 F. Weigend and R. Ahlrichs, Balanced basis sets of split valence, triple zeta valence and quadruple zeta valence quality for H to Rn: Design and assessment of accuracy, *Phys. Chem. Chem. Phys.*, 2005, **7**, 3297–3305.
32 F. Neese, Software update: the ORCA program system, version 5.0, *WIRES Comput. Molec. Sci.*, 2022, **12**(1), e1606.
33 D. Andrae, U. Häußermann, M. Dolg, H. Stoll and H. Preuß, Energy-Adjusted ab initio Pseudopotentials for the Second and Third Row Transition Elements, *Theoret. Chim. Acta*, 1990, **77**, 123–141.
34 S. Hirata and M. Head-Gordon, Time-dependent density functional theory within the Tamm Dancoff approximation, *Chem. Phys. Lett.*, 1999, **314**, 291–299.
35 A. Dreuw and M. Head-Gordon, Single-Reference ab Initio Methods for the Calculation of Excited States of Large Molecules, *Chem. Rev.*, 2005, **105**, 4009–4037.
36 B. Moore, H. Sun, N. Govind, K. Kowalski and J. Autschbach, Charge-Transfer Versus Charge-Transfer-Like Excitations Revisited, *J. Chem. Theory Comput.*, 2015, **11**, 3305–3320.
37 J. Feng, L. Yang, A. S. Romanov, J. Ratanapreechachai, A.-P. M. Reponen, S. T. E. Jones, M. Linnolahti, T. J. H. Hele, A. Köhler, H. Bässler, M. Bochmann and D. Credgington, Environmental Control of Triplet Emission in Donor–Bridge–Acceptor Organometallics, *Adv. Funct. Mater.*, 2020, **30**, 1908715.
38 T. Lu and F. Chen, Multiwfn: A multifunctional wavefunction analyzer, *J. Comput. Chem.*, 2012, **33**, 580–592.
39 T. Chen, L. Zheng, J. Yuan, Z. An, R. Chen, Y. Tao, H. Li, X. Xie and W. Huang, Understanding the Control of Singlet-Triplet Splitting for Organic Exciton Manipulating: A Combined Theoretical and Experimental Approach, *Sci. Rep.*, 2015, **5**, 10923.
40 T. Pope, Y. Giret, M. Fsadni, P. Docampo, C. Groves and T. J. Penfold, Modelling the effect of dipole ordering on charge-carrier mobility in organic semiconductors, *Org. Electron.*, 2023, **115**, 106760.
41 A.-P. M. Reponen, G. Londi, C. S. B. Matthews, Y. Olivier, A. S. Romanov, N. C. Greenham and A. J. Gillett, Understanding Spin-Triplet Excited States in Carbene-Metal-Amides, *Angew. Chem., Int. Ed.*, 2024, **63**, e202402052.
42 Y. Liu, C. Li, Z. Ren, S. Yan and M. Bryce, All-organic thermally activated delayed fluorescence materials for organic light-emitting diodes, *Nat. Rev. Mater.*, 2018, **3**, 18020.
43 J. R. Gispert, *Coordination Chemistry*, Wiley–VCH, Weinheim, Germany, 2008, 483.
44 G. Bao, R. Y. Abe and Y. Akutsu, Bond dissociation energy and thermal stability of energetic materials, *J. Therm. Anal. Calorim.*, 2021, **143**, 3439–3445.
45 National Center for Biotechnology Information. PubChem Compound Summary for CID 6736, Skatole. **https://pubchem.ncbi.nlm.nih.gov/compound/Skatole**. Accessed Apr. 12, 2025.
46 National Center for Biotechnology Information. PubChem Compound Summary for CID 10328, Indoline. **https://pubchem.ncbi.nlm.nih.gov/compound/Indoline**. Accessed Apr. 12, 2025.
47 National Center for Biotechnology Information. PubChem Compound Summary for CID 5281404, Harman. **https://pubchem.ncbi.nlm.nih.gov/compound/Harman**. Accessed Apr. 12, 2025.
48 National Center for Biotechnology Information. PubChem Compound Summary for CID 1868, 6-Methoxytryptoline. **https://pubchem.ncbi.nlm.nih.gov/compound/6-Methoxytryptoline**. Accessed Apr. 12, 2025.
49 A. Endo, M. Ogasawara, A. Takahashi, D. Yokoyama, Y. Kato and C. Adachi, Thermally activated delayed fluorescence from Sn^{4+}-porphyrin complexes and their application to organic light emitting diodes - A novel mechanism for electroluminescence, *Adv. Mater.*, 2009, **21**, 4802–4806.
50 (*a*) CCDC 2454948: Experimental Crystal Structure Determination. DOI: **10.5517/ccdc.csd.cc2ndkwj**; (*b*) CCDC 2454949: Experimental Crystal Structure Determination. DOI: **10.5517/ccdc.csd.cc2ndkxk**.